



CHORUS

This is the accepted manuscript made available via CHORUS. The article has been published as:

Measurements of the temperature and velocity of the dense fuel layer in inertial confinement fusion experiments

O. M. Mannion, A. J. Crilly, C. J. Forrest, B. D. Appelbe, R. Betti, V. Yu. Glebov, V. Gopalaswamy, J. P. Knauer, Z. L. Mohamed, C. Stoeckl, J. P. Chittenden, and S. P. Regan

Phys. Rev. E **105**, 055205 — Published 12 May 2022

DOI: [10.1103/PhysRevE.105.055205](https://doi.org/10.1103/PhysRevE.105.055205)

Measurements of the Temperature and Velocity of the Dense Fuel Layer in Inertial Confinement Fusion Experiments

O. M. Mannion,^{1,*} A. J. Crilly,² C. J. Forrest,¹ B. D. Appelbe,² R. Betti,¹ V. Yu. Glebov,¹ V. Gopalaswamy,¹ J. P. Knauer,¹ Z. L. Mohamed,¹ C. Stoeckl,¹ J. P. Chittenden,² and S. P. Regan¹

¹*Laboratory for Laser Energetics, University of Rochester, Rochester, NY 14623*

²*Centre for Inertial Fusion Studies, The Blackett Laboratory, Imperial College, London SW72AZ*

The apparent ion temperature and mean velocity of the dense deuterium tritium fuel layer of an inertial confinement fusion target near peak compression have been measured using backscatter neutron spectroscopy. The average isotropic residual kinetic energy of the dense DT fuel is estimated using the mean velocity measurement to be ~ 103 J across an ensemble of experiments. The apparent ion-temperature measurements from high implosion velocity experiments are larger than expected from radiation-hydrodynamic simulations and are consistent with enhanced levels of shell decompression. These results suggest that high-mode instabilities may saturate the scaling of implosion performance with the implosion velocity for laser-direct-drive implosions.

I. INTRODUCTION

In the laser-driven inertial confinement fusion (ICF) [1] experiments performed at the National Ignition Facility (NIF) [2, 3] and on the OMEGA-60 laser [4], a spherical capsule, filled with a deuterium tritium (DT) vapor that is surrounded by a dense DT ice layer is imploded by irradiating the target with a high-power laser. At peak compression, a low-density (~ 20 -g/cm³), high-temperature (~ 5 -keV) thermonuclear hot-spot plasma is formed, which is surrounded by a low-temperature (~ 500 -eV), high-density (~ 200 -g/cm³) DT fuel layer [see Fig. 1(a)]. The goal of these experiments is to study the feasibility of generating an igniting plasma [5, 6] in which a thermonuclear burn wave is propagated from the hot spot into the dense DT fuel layer, resulting in the generation of a large fusion yield.

Measurements of the hot-spot apparent ion temperature [7], electron temperature [8], bulk velocity [9, 10], volume [11, 12], target areal density [13], and shape of the dense DT fuel layer [12, 14] near peak compression are routinely obtained in ICF experiments and are used to assess implosion performance [15]. The hydrodynamic properties of the dense DT fuel near peak compression, however, have been largely undiagnosed in ICF experiments, leaving the temperature and velocity in this region of the target uncertain [16]. The temperature of the dense DT fuel layer is a key implosion parameter since the entropy of the fuel must be kept as low as possible in order to achieve the high levels of compression required for ignition [17]. Furthermore, the velocity of the dense DT fuel layer near peak compression is key for understanding the amount of residual kinetic energy [18–20] not used to heat and compress the target.

Recent theoretical work [21, 22] has demonstrated how the ion velocity distribution within a dense material can

be studied by measuring the backscattered neutron energy spectrum generated when incident neutrons scatter off a material. This technique relies on the fact that when an incident neutron with velocity v_n elastically backscatters (i.e., $\theta = \pi$) off an ion with a parallel velocity v_i , the neutron will exit the scattering event with a velocity $v'_n = [(A - 1)v_n + 2Av_i] / (A + 1)$ [22], where A is the ion-to-neutron mass ratio [see Figs. 1(a) and 1(b)]. If both the incident neutrons and the scattering ions have a velocity distribution, as will be the case in ICF experiments, the mean neutron backscatter velocity will be given by $\langle v'_n \rangle = [(A - 1)\langle v_n \rangle + 2A\langle v_i \rangle] / (A + 1)$ and the neutron backscatter velocity variance will given by $\text{Var}(v'_n) = [(A - 1)\text{Var}(v_n) + 2A\text{Var}(v_i)] / (A + 1)$, where the mean $\langle \rangle$ and variance $\text{Var}()$ are calculated over the respective neutron and ion velocity distributions [22]. If both the incident and backscattered neutron velocity spectrum are measured in an experiment, then the mean (i.e., drift velocity) and variance (i.e., apparent ion temperature [23, 24]) of the ion velocity distribution can be inferred from measurements of the backscatter neutron velocity (energy) spectrum.

In this article, measurements of the neutron tritium (nT) backscatter edge from an ICF experiment are used to infer the mean velocity and apparent ion temperature of the dense DT fuel layer near peak compression. The average isotropic residual kinetic energy in the fuel layer near peak compression is estimated to be ~ 103 J using the mean velocity measurements. The apparent ion temperature of the dense fuel layer is observed to increase with the peak implosion velocity of the experiment at a higher rate than expected. The apparent ion temperature measurement, along with several other diagnostic measurements, is consistent with enhanced levels of shell decompression in high implosion velocity experiments, which are shown to be more susceptible to shell decompression from high-mode instabilities during the acceleration phase. These results suggest that high-mode instabilities may saturate the scaling of implosion performance with the implosion velocity for laser-direct-drive implosions performed on OMEGA.

* Present address: Sandia National Laboratories, Albuquerque, New Mexico 87185, USA

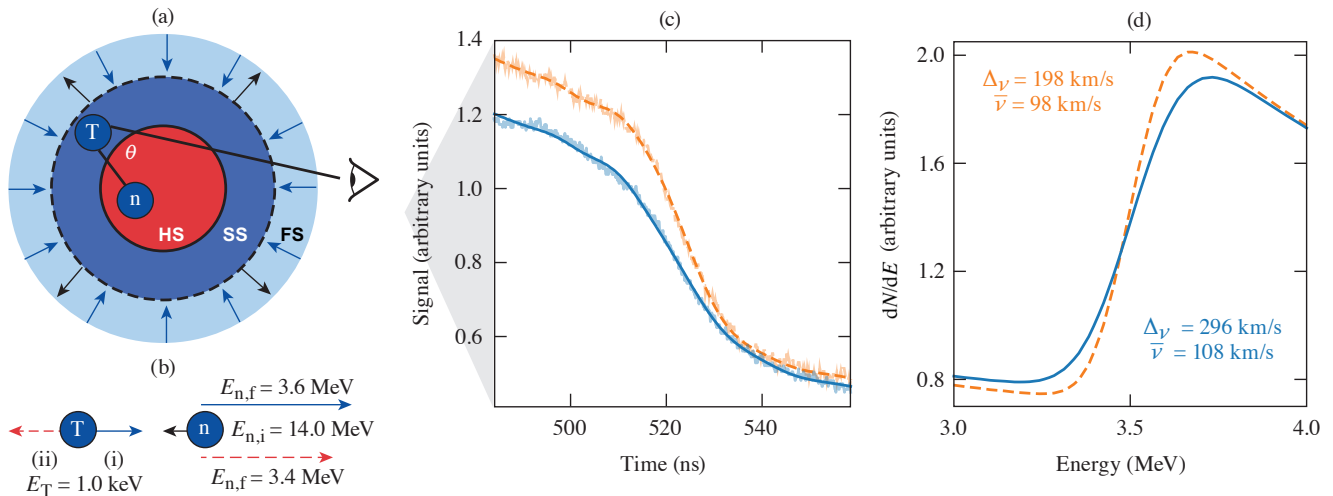


FIG. 1. (a) A schematic of neutron scattering in an ICF target near peak compression that consists of a central low-density, high-temperature hot spot (HS, red), surrounded by a low-temperature, high-density shocked shell (SS, blue), which is surrounded by a low-density and temperature free-falling shell (FS, light blue) which is still imploding radially inward. A rebounding shock (dashed line) separates the shocked shell and free-falling material and propagates radially outward. (b) An example of the neutron tritium backscatter kinematics assuming the tritium has 1 keV of kinetic energy and moves toward (blue solid arrow) or away (red dashed arrow) from the incident neutron. (c) Two nT edge neutron time-of-flight signals (shaded curves) from OMEGA implosions along with the forward fit (solid and dashed lines). (d) The unfolded neutron energy spectra used to forward fit the data in (c), along with the best fit values for the mean \bar{v} and standard deviation Δv of the tritium velocity distribution used in the forward fit. The signals in (c) and (d) have been normalized to the primary DT yield to highlight the shape differences.

II. EXPERIMENTAL ANALYSIS

Measurements of the nT edge were obtained during a series of cryogenic laser-direct-drive ICF implosions performed on the 60-beam, 30-kJ, 351-nm OMEGA laser [4]. The implosions used a variety of different laser and target designs meant to optimize the primary DT fusion yield and areal density (ρR) of the implosions [25]. The primary DT yields of these experiments ranged from 3.8×10^{13} to 1.5×10^{14} with ρR values between 92 and 176 mg/cm². To minimize the effect of low-mode implosion asymmetries [26–28], only experiments with hot-spot apparent ion temperature asymmetries <0.8 keV [29] and hot-spot flow [10] velocities <80 km/s were considered.

The nT edge measurements were obtained using a neutron time-of-flight (nTOF) spectrometer [30] located 13.35 m from the target chamber center in a well-collimated line of sight (LOS). The nTOF detector consists of a liquid xylene scintillator coupled to four photomultiplier tubes, which are used in current mode to record the spectrum of neutron arrival times [31, 32]. Two example nTOF data sets recorded by this detector are shown in Fig. 1(c).

The measured nTOF data were forward fit [7] using a model neutron energy spectrum [22], which includes the DT, DD, and TT primary fusion reactions [33–35], the neutron tritium (nT) and neutron deuterium (nD) elastic scattering reactions, and the inelastic deuteron breakup reaction [36]. The shape of the nT elastic neutron energy

spectrum was calculated assuming the tritium velocity distribution has a normal distribution with a mean velocity \bar{v} and variance Δv^2 , while all other scattering reactions assume the scattering medium is static. The mean and variance of the primary neutron energy spectrum were measured using a separate nTOF detector located adjacent to the xylene detector [37]. The detector instrument response function, line-of-sight attenuation, sensitivity, and backgrounds have been constructed by combining calibration measurements and neutron transport calculations using the Monte Carlo code MCNP [7, 38–40].

Detector backgrounds due to the large DT neutron signal in these experiments [41] were characterized by measuring the nTOF signal produced from a set of DT-filled glass exploding-pusher experiments [42] with primary DT yields ranging from 3×10^{13} to 1.6×10^{14} and areal densities <10 mg/cm². The low areal density in these experiments results in negligible scattering of the primary fusion neutrons in the target and so the detector backgrounds can be determined from the residual nTOF signal not accounted for by the primary fusion neutrons. The measured signals were forward fit with the same neutron energy spectrum model used in the nT edge analysis with the addition of an exponential decay background model. The amplitude and decay constant of the exponential decay background were determined for each experiment. It was found that the amplitude of the background scales linearly with the primary DT yield, while the decay constant is fixed. In subsequent analyses

TABLE I. Summary of the uncertainties from a sensitivity study and from the covariance matrix of the fit.

Source	\bar{v} (km/s)	Δ_v (km/s)
Detector sensitivity model	30	10
Fit region	6	14
Detector IRF	5	2
Hot-spot velocity	5	0
Hot-spot T_i	0	1
Total Systematic	31	17
Total Statistical	2	4
Total	33	21

of the nT edge in cryogenic experiments, this background is included in the forward model with the experimentally determined decay constant held fixed and the amplitude as a free parameter.

Two example nT edge measurements are shown in Fig. 1(c) along with the forward model used to fit the data. The slope of the edge, which represents the triton velocity distribution variance Δ_v^2 , is observed to change between experiments, while the position of the edge, which represents the triton velocity distribution mean \bar{v} , are similar. The neutron energy spectra used to fit the nTOF data are shown in Fig. 1(d).

Table I summarizes the systematic and statistical uncertainty in the values of \bar{v} and Δ_v inferred from the fit. The systematic uncertainty in the measured values arise from the detector sensitivity, fit region, detector IRF shape, the modeled beamline attenuation, as well as the measured primary DT spectrum used in the nT edge model. The contribution from each of these components were estimated from a sensitivity study in which a series of forward fits were performed by adding perturbations to each potential uncertainty source. The systematic uncertainty was then estimated from the range of inferred values generated from these fits. The statistical uncertainty in the measured values were determined from the fit covariance matrix. Table I shows that the error in the inferred values are dominated by systematic sources of uncertainty.

III. RESULTS

Figure 2(a) shows the inferred values of \bar{v} and Δ_v as functions of the peak implosion velocity, u_{imp} , for the ensemble of experiments considered in this work. The peak implosion velocity was calculated from post-shot simulations using the 1-D radiation-hydrodynamic code *LILAC* [43] using the as-shot target and laser conditions. The implosion velocity from *LILAC* has been benchmarked in previous experiments [44] and the simulated bang times agree with the measured values. For each post-shot simulation, the predicted values of Δ_v and \bar{v} were calculated by taking the moments of the simulated scatter-weighted triton velocity distribution [22]. Both Δ_v and \bar{v} were found

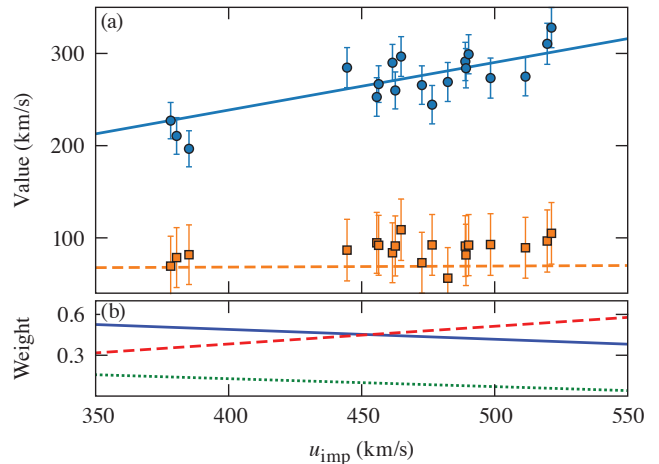


FIG. 2. (a) The measured (points) and LILAC calculated (lines) values for Δ_v (blue points and solid line) and \bar{v} (orange squares and dashed line) as functions of the calculated peak implosion velocity. (b) The *LILAC* calculated scattering fraction occurring in the hot spot (red), shocked shell (dark blue), and free-falling shell (green) as functions of the calculated peak implosion velocity.

to have a linear relationship with u_{imp} as shown in Fig. 2.

In order to interpret these results it is important to note that the nT edge measures the scatter-weighted triton velocity distribution of the implosion in both space and time [22], and thereby contains information on the triton velocity distribution throughout the entire target. At peak compression a typical ICF experiment has three distinct regions: the hot spot, shocked shell, and free-falling shell [45] [see Fig. 1(a)]. The average triton velocity distribution in the i^{th} region of the target is well described by a normal distribution with a mean \bar{v}_i and variance $\Delta_{v,i}^2$ which is determined by the local hydrodynamic properties in the region [22]. The total scatter-weighted triton distribution is the sum of the triton velocity distribution in each region of the target, weighted by the amount of scattering occurring within each region, which is given by $w_i = (\rho R)_i / \rho R$. The mean of the total scatter-weighted ion distribution is given by $\bar{v} = \sum_i w_i \bar{v}_i$, while the variance is given by $\Delta_v^2 = \sum_i w_i \Delta_{v,i}^2 + \left(\sum_i w_i \bar{v}_i^2 - \bar{v}^2 \right)$ [22].

Near peak compression, the hot-spot region has a high ion temperature (~ 5 keV) and has stagnated, and therefore has a broad thermal triton velocity distribution centered around zero. Throughout the compression, the shocked shell has a low ion temperature (≤ 500 eV) but has a mean velocity near the implosion velocity at the beginning of the deceleration phase and eventually comes to stagnation at peak compression. As a result, the shocked-shell triton distribution has a large nonthermal velocity variance proportional to the deceleration of the shell during the deceleration phase. Finally, the free-falling shell

has a low ion temperature (~ 50 eV) and is still imploding at the implosion velocity, resulting in a narrow triton velocity distribution with a mean near the implosion velocity.

Since the mean velocity in the hot spot is $\bar{v}_{\text{hs}} \approx 0$, the total measured \bar{v} can be interpreted as the average velocity of the shocked shell and free-falling shell near peak compression. Therefore the kinetic energy of the shell near peak compression can be estimated from the \bar{v} measurement using the expression $1/2M_{\text{sh}}\bar{v}^2$, where M_{sh} is the shell mass. The shell mass is estimated using $M_{\text{sh}} = M_{\text{init}} - M_{\text{hs}}$, where M_{init} is the initial mass of the DT vapor and ice layer and M_{hs} is the experimentally inferred hot-spot mass [15]. The inferred shell mass values ranged from 23 to 30 μg . Combining this with the measured values of \bar{v} (see Fig. 2(a)), the average shell isotropic residual kinetic energy is calculated to be 103 J. This represents $\sim 10\%$ of the peak shell kinetic energy, which is ~ 1 kJ for OMEGA implosion designs [46]. This result is consistent with moderately perturbed radiation-hydrodynamic simulation results [46] and is the first direct measurement of residual kinetic energy in the shell near peak compression. The weak linear dependence of \bar{v} on u_{imp} (see Fig. 2(a)) suggest that the isotropic residual kinetic energy in these implosions is systematic.

In order to understand the linear relationship observed between Δ_v and u_{imp} it is important to note that the amount of scattering occurring within the hot spot increases linearly with the peak implosion velocity while the scattering occurring with the shocked and free-falling shell decreases linearly with the peak implosion velocity (see Fig. 2(b)). The increase in the amount of hot-spot scattering with implosion velocity results from the fact that faster implosions generate higher hot-spot temperatures [47], which increases the rate at which mass is ablated from the dense fuel into the hot spot through thermal conduction [48, 49]. Furthermore, increasing the peak implosion velocity increases the velocity of the rebounding shock responsible for forming the shocked shell region. When this shock travels faster, it results in more of the shell being shocked by the time of peak compression, resulting in less free-falling material. The linear increase in the measured Δ_v is primarily a result of the linear increase in the amount of scattering occurring within the hot spot, which, as mentioned above, has a large thermal triton velocity variance, which skews the measurement more toward the hot-spot thermal velocity variance.

A hot-spot model [15, 50–52] has been used to eliminate the hot-spot contribution to the measured Δ_v values such that the conditions of the dense fuel layer can be studied. The hot spot is assumed to be isobaric with a pressure P_{hs} with a temperature profile $T(r) = T_0 [1 - \epsilon(r/R_{\text{hs}})^2]^\beta$, where T_0 is the peak ion temperature, r is the radius, $R_{\text{hs}} = 1.06R_{17}$ [51], R_{17} is the 17% contour of the measured hot-spot image near peak compression [11], $\beta = 2/3$ is a shape metric related to the thermal conductivity in the hot spot [15], and $\epsilon = (1 - 0.15^{1/\beta})$ is

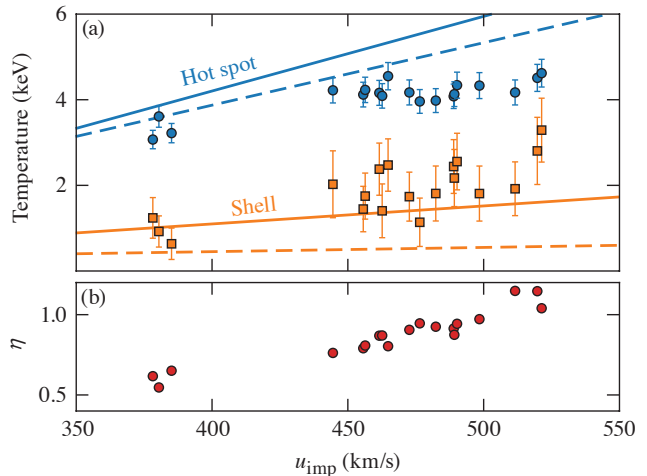


FIG. 3. (a) The hot-spot (upper blue points and lines) and shell (lower orange squares and lines) ion temperature as a function of the peak implosion velocity. The calculated thermal ion temperature (dashed lines) and apparent ion temperature (solid lines) are calculated using *LILAC* while the measured apparent ion temperature (points and squares) are inferred from the nTOF spectrum. (b) The relationship between the implosion stability metric η and the peak implosion velocity.

a shape correction factor used to match more-complete radiation-hydrodynamic profiles [51, 52]. P_{hs} and T_0 are determined by matching the measured fusion yield and minimum apparent hot-spot temperature [15] using the measured nuclear production history, which has a temporal width τ . The hot-spot temperature profile is related to the hot-spot density profile using the isobaric pressure P_{hs} .

The hot-spot profile has been inferred for each of the experiments, and the hot-spot areal density $(\rho R)_{\text{hs}}$, triton velocity variance $\Delta_{v,\text{hs}}$, and scattering fraction $w_{\text{hs}} = (\rho R)_{\text{hs}}/\rho R$ were calculated using the measured areal density [53]. The velocity variance of the shell can be inferred by subtracting the hot-spot contribution and is given by $\Delta_{v,\text{sh}}^2 = (\Delta_v^2 - w_{\text{hs}}\Delta_{v,\text{hs}}^2)/(1 - w_{\text{hs}})$ [54]. Here $\Delta_{v,\text{sh}}$ is the weighted average of the shocked shell and free-falling shell contribution. In deriving the expression for $\Delta_{v,\text{sh}}^2$ [54] the nonthermal (i.e., shell motion) velocity variance contribution to the total triton velocity measurement has been neglected because it cannot currently be measured experimentally. This assumption will lead to the inferred values of Δ_v^2 being slightly larger than exact value. Applying the above expression to *LILAC* data resulted in inferred shell velocity variances 20% larger than the exact value. The apparent ion temperature, a quantity sensitive to both thermal and nonthermal motion of the shell, is inferred using the shell velocity variance as $T_{\text{sh}} = m_T \Delta_{v,\text{sh}}^2$, where m_T is the mass of a triton [22].

Figure 3(a) shows the measured and simulated apparent and thermal shell temperatures for both the hot spot and shell. The simulated thermal temperatures were de-

terminated by calculating the neutron averaged temperature for the hot spot and the scatter-weighted temperature in the shell. The simulated hot spot apparent ion temperatures were calculated by adding fluid velocity broadening to the thermal ion temperature [19]. The simulated apparent shell temperatures were calculated from the simulated shell velocity variance ($\Delta_{v,sh}^2$) using the method described above. The difference between the simulated thermal and apparent temperature is caused by the nonthermal motion in the implosion (i.e., shell deceleration or hot-spot radial motion). The measured shell apparent ion temperatures are greater than predicted by *LILAC* for the high implosion velocity (>450-km/s) experiments, while the measured hot-spot apparent ion temperatures are lower than predicted. The higher apparent shell temperatures suggest larger than predicted nonthermal flow velocity variances within the shell near peak compression. In comparison, the lower apparent hot-spot temperatures indicate that the conversion of the shell kinetic energy to hot-spot thermal energy becomes less efficient for high implosion velocity experiments. Low-mode asymmetries are expected to increase the flow velocity variances in the shell and hot spot but are unlikely to cause the observed trend since these implosions were chosen because they show no gross apparent ion temperature asymmetry or hot-spot velocity. Therefore the larger flow velocity variances are likely the result of a high-mode degradation mechanism.

The apparent hot-spot and shell temperature observations are consistent with enhanced levels of shell decompression for the high-implosion velocity experiments. Shell decompression [44] is caused by the growth of Rayleigh-Taylor (RT) instabilities, seeded by laser imprint [55] and target defects [56], into the shell during the acceleration phase of the implosion and increases the shell thickness in flight [57, 58]. As the target converges, a rebounding shock propagates radially outward from the hot spot to the shell and initiates the deceleration phase of the implosion (see Fig. 1(a)). Since the rebounding shock velocity and implosion time scale are approximately the same for a compressed or decompressed shell, an implosion with a decompressed shell will have less shocked shell and more free-falling material at peak compression. This increases the apparent shell temperature as the excess of free-falling shell material increases the total shell velocity variance [22]. Furthermore, since only the shocked portion of the shell performs PdV work on the hot spot [45], less of the shell's kinetic energy will be converted into thermal energy of the hot spot, resulting in lower hot-spot temperatures.

The ratio between the depth that RT bubbles travel into the shell, h_b , and the shell thickness, Δ , is a metric for how susceptible an implosion is to shell decompression and can be used to test the shell decompression hypothesis. After a time t , a fully developed non-linear RT bubble will travel a distance $h_b = \alpha_b g t^2$ into the shell, where α_b is dimensionless quantity that characterizes the bubble front growth [59] and g is the shell acceleration.

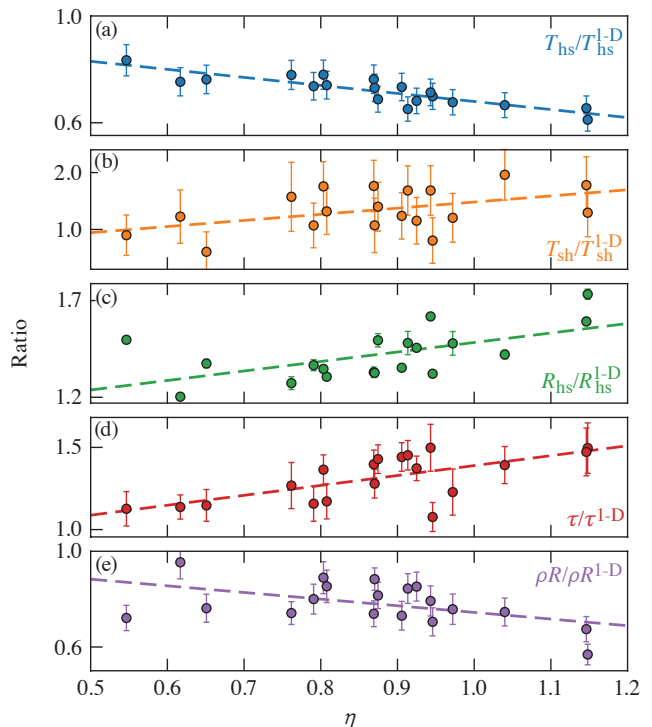


FIG. 4. The ratio between the measured and simulated values for various physics parameters a function of the implosion stability metric η . The dashed lines are linear fit for each parameter.

It is easy to show [47] that the ratio of the shell thickness and the bubble penetration depth at some later point in time is given by $\eta = h_b/\Delta = 2\alpha_b \text{IFAR}(\text{CR} - 1)$, where $\text{IFAR} = R/\Delta$ is the in-flight aspect ratio, $\text{CR} = R_0/R$ is the convergence ratio, and R_0 is the target initial radius. The maximum value of η during the acceleration phase was calculated from post-shot *LILAC* simulations for each experiment and are shown in Fig. 3(b). This simplified model will overestimate the amount of shell decompression since it takes time for the bubble front to develop and does not account for ablative stabilization, but does provide a useful metric for shell decompression.

Figure 3(b) shows that η increases rapidly with the peak implosion velocity for the implosion designs considered in this work, suggesting that higher implosion velocity experiments are more susceptible to shell decompression. This is a direct consequence of the fact that the high implosion velocities are typically achieved by using larger targets with thinner ice layer [25], which increases the initial aspect ratio of the shell, making them more susceptible to shell breakup.

The degradation in several key experimental observables as a function of η is shown in Fig. 4 and supports the decompression hypothesis. In particular, Fig. 4(a) shows that the ratio between the measured and simulated apparent hot-spot temperatures decreases linearly with η , indicating lower hot-spot temperatures are achieved

as the shell becomes more decompressed and inefficiently converts its kinetic energy to hot-spot thermal energy. Figure 4(b) shows that the ratio between the measured and simulated apparent shell temperatures increases linearly with η , indicating larger-than-expected flow velocity variances within the shell caused by the larger than predicted amount of free-falling shell material. Figure 4(c) shows that larger hot spots are observed in implosions with higher values of η , which is consistent with predictions from radiation-hydrodynamic simulations of implosions with decompressed shell [60]. Figure 4(d) shows that the ratio of the measured and simulated nuclear production history width increases linearly with η , which is expected as decompressed shells produce lower hot-spot pressures, which results in a slower expansion of the shell material [61]. Finally, Fig. 4(e) shows that lower-than-expected areal densities are observed from implosions with higher values of η .

IV. SUMMARY

In conclusion, the mean velocity and apparent ion temperature of the dense DT fuel layer near peak compression were measured for the first time using a novel neutron backscatter technique. The mean velocity measurements were used to infer the isotropic residual kinetic energy of the shell near peak compression. The apparent ion temperature of the fuel layer in high implosion velocity experiments was observed to be higher than expected from 1-D radiation-hydrodynamic codes, while the apparent hot-spot temperature was lower than expected. It was shown that higher implosion velocity experiments are more susceptible to shell decompression for the implosion designs considered in this work. Several experimental observables show evidence of enhanced level of decompression for the high implosion velocity experiments and support this claim. These results suggest a plateau exists in the scaling of LDD implosion performance with implosion velocity and must be considered by implosion designers.

Future work will extend this analysis to multiple LOS

and investigate asymmetric implosions. Additionally, this technique can be applied to other backscatter edges that occur in ICF experiments such as those observed in laser indirect drive implosions performed on the NIF or magnetized liner inertial fusion experiments performed on the Z machine.

ACKNOWLEDGMENTS

This material is based upon work supported by the Department of Energy National Nuclear Security Administration under Award Number DE-NA0003856, the University of Rochester, and the New York State Energy Research and Development Authority.

Sandia National Laboratories is a multimission laboratory managed and operated by National Technology & Engineering Solutions of Sandia, LLC, a wholly owned subsidiary of Honeywell International Inc., for the U.S. Department of Energy's National Nuclear Security Administration under contract DE-NA0003525. This paper describes objective technical results and analysis. Any subjective views or opinions that might be expressed in the paper do not necessarily represent the views of the U.S. Department of Energy or the United States Government.

This report was prepared as an account of work sponsored by an agency of the U.S. Government. Neither the U.S. Government nor any agency thereof, nor any of their employees, makes any warranty, express or implied, or assumes any legal liability or responsibility for the accuracy, completeness, or usefulness of any information, apparatus, product, or process disclosed, or represents that its use would not infringe privately owned rights. Reference herein to any specific commercial product, process, or service by trade name, trademark, manufacturer, or otherwise does not necessarily constitute or imply its endorsement, recommendation, or favoring by the U.S. Government or any agency thereof. The views and opinions of authors expressed herein do not necessarily state or reflect those of the U.S. Government or any agency thereof.

-
- [1] J. Nuckolls, L. Wood, A. Thiessen, and G. Zimmerman, *Nature* **239**, 139 (1972).
 - [2] E. I. Moses, *J. Phys. Conf. Ser.* **112**, 012003 (2008).
 - [3] M. J. Edwards, P. K. Patel, J. D. Lindl, L. J. Atherton, S. H. Glenzer, S. W. Haan, J. D. Kilkenny, O. L. Landen, E. I. Moses, A. Nikroo, *et al.*, *Phys. Plasmas* **20**, 070501 (2013).
 - [4] T. R. Boehly, D. L. Brown, R. S. Craxton, R. L. Keck, J. P. Knauer, J. H. Kelly, T. J. Kessler, S. A. Kumpan, S. J. Loucks, S. A. Letzring, *et al.*, *Opt. Commun.* **133**, 495 (1997).
 - [5] R. Betti and O. A. Hurricane, *Nat. Phys.* **12**, 435 (2016).
 - [6] A. R. Christopherson, R. Betti, S. Miller, V. Gopalaswamy, O. M. Mannion, and D. Cao, *Phys. Plasmas* **27**, 052708 (2020).
 - [7] R. Hatarik, D. B. Sayre, J. A. Caggiano, T. Phillips, M. J. Eckart, E. J. Bond, C. J. Cerjan, G. P. Grim, E. P. Hartouni, J. P. Knauer, *et al.*, *J. Appl. Phys.* **118**, 184502 (2015).
 - [8] L. C. Jarrott, B. Bachmann, T. Ma, L. R. Benedetti, F. E. Field, E. P. Hartouni, R. Hatarik, N. Izumi, S. F. Khan, O. L. Landen, *et al.*, *Phys. Rev. Lett.* **121**, 085001 (2018).
 - [9] R. Hatarik, R. C. Nora, B. K. Spears, M. J. Eckart, G. P. Grim, E. P. Hartouni, A. S. Moore, and D. J. Schlossberg, *Rev. Sci. Instrum.* **89**, 101138 (2018).

- [10] O. M. Mannion, J. P. Knauer, V. Y. Glebov, C. J. Forrest, A. Liu, Z. L. Mohamed, M. H. Romanofsky, T. C. Sangster, C. Stoeckl, and S. P. Regan, *Nucl. Instruments Methods Phys. Res. Sect. A Accel. Spectrometers, Detect. Assoc. Equip.* **964**, 163774 (2020).
- [11] F. J. Marshall, R. E. Bahr, V. N. Goncharov, V. Y. Glebov, B. Peng, S. P. Regan, T. C. Sangster, and C. Stoeckl, *Rev. Sci. Instrum.* **88**, 093702 (2017).
- [12] G. P. Grim, N. Guler, F. E. Merrill, G. L. Morgan, C. R. Danly, P. L. Volegov, C. H. Wilde, D. C. Wilson, D. S. Clark, D. E. Hinkel, *et al.*, *Phys. Plasmas* **20**, 056320 (2013).
- [13] C. J. Forrest, P. B. Radha, V. Y. Glebov, V. N. Goncharov, J. P. Knauer, A. Pruyne, M. Romanofsky, T. C. Sangster, M. J. Shoup, C. Stoeckl, *et al.*, *Rev. Sci. Instrum.* **83**, 10D919 (2012).
- [14] P. L. Volegov, S. H. Batha, V. Geppert-Kleinrath, C. R. Danly, F. E. Merrill, C. H. Wilde, D. C. Wilson, D. T. Casey, D. Fittinghoff, B. Appelbe, *et al.*, *J. Appl. Phys.* **127**, 083301 (2020).
- [15] P. K. Patel, P. T. Springer, C. R. Weber, L. C. Jarrott, O. A. Hurricane, B. Bachmann, K. L. Baker, L. F. Berzak Hopkins, D. A. Callahan, D. T. Casey, *et al.*, *Phys. Plasmas* **27**, 050901 (2020).
- [16] A. C. Hayes, M. E. Gooden, E. Henry, G. Jungman, J. B. Wilhelmy, R. S. Rundberg, C. Yeamans, G. Kyrala, C. Cerjan, D. L. Danielson, *et al.*, *Nat. Phys.* **258**, 1 (2020).
- [17] J. Lindl, *Phys. Plasmas* **2**, 3933 (1995).
- [18] B. K. Spears, M. J. Edwards, S. P. Hatchett, J. Kilkenny, J. Knauer, A. Kritcher, J. Lindl, D. Munro, P. Patel, H. F. Robey, *et al.*, *Phys. Plasmas* **21**, 042702 (2014).
- [19] K. M. Woo, R. Betti, D. Shvarts, A. Bose, D. Patel, R. Yan, P.-Y. Chang, O. M. Mannion, R. Epstein, J. A. Delettretz, *et al.*, *Phys. Plasmas* **25**, 052704 (2018).
- [20] A. Bose, R. Betti, D. Mangino, K. M. Woo, D. Patel, A. R. Christopherson, V. Gopalaswamy, O. M. Mannion, S. P. Regan, V. N. Goncharov, *et al.*, *Phys. Plasmas* **25**, 062701 (2018).
- [21] A. J. Crilly, B. D. Appelbe, K. McGlinchey, C. A. Walsh, J. K. Tong, A. B. Boxall, and J. P. Chittenden, *Phys. Plasmas* **25**, 122703 (2018).
- [22] A. J. Crilly, B. D. Appelbe, O. M. Mannion, C. J. Forrest, V. Gopalaswamy, C. A. Walsh, and J. P. Chittenden, *Phys. Plasmas* **27**, 012701 (2020).
- [23] T. J. Murphy, R. E. Chrien, and K. A. Klare, *Rev. Sci. Instrum.* **68**, 614 (1997).
- [24] T. J. Murphy, *Phys. Plasmas* **21**, 072701 (2014).
- [25] V. Gopalaswamy, R. Betti, J. P. Knauer, N. Luciani, D. Patel, K. M. Woo, A. Bose, I. V. Igumenshchev, E. M. Campbell, K. S. Anderson, *et al.*, *Nature* **565**, 581 (2019).
- [26] H. G. Rinderknecht, D. T. Casey, R. Hatarik, R. M. Bionta, B. J. MacGowan, P. Patel, O. L. Landen, E. P. Hartouni, and O. A. Hurricane, *Phys. Rev. Lett.* **124**, 145002 (2020).
- [27] D. T. Casey, B. J. MacGowan, J. D. Sater, A. B. Zylstra, O. L. Landen, J. Milovich, O. A. Hurricane, A. L. Kritcher, M. Hohenberger, K. Baker, *et al.*, *Phys. Rev. Lett.* **126**, 25002 (2021).
- [28] O. M. Mannion, I. V. Igumenshchev, K. S. Anderson, R. Betti, E. M. Campbell, D. Cao, C. J. Forrest, M. G. Johnson, V. Y. Glebov, V. N. Goncharov, *et al.*, *Phys. Plasmas* **28**, 042701 (2021).
- [29] O. M. Mannion, K. M. Woo, A. J. Crilly, C. J. Forrest, J. A. Frenje, M. G. Johnson, V. Y. Glebov, J. P. Knauer, Z. L. Mohamed, M. H. Romanofsky, *et al.*, *Rev. Sci. Instrum.* **92**, 033529 (2021).
- [30] R. A. Lerche, L. W. Coleman, J. W. Houghton, D. R. Speck, and E. K. Storm, *Appl. Phys. Lett.* **31**, 645 (1977).
- [31] V. Y. Glebov, C. J. Forrest, K. L. Marshall, M. Romanofsky, T. C. Sangster, M. J. Shoup, and C. Stoeckl, *Rev. Sci. Instrum.* **85**, 11E102 (2014).
- [32] C. J. Forrest, V. Y. Glebov, V. N. Goncharov, J. P. Knauer, P. B. Radha, S. P. Regan, M. H. Romanofsky, T. C. Sangster, M. J. Shoup, and C. Stoeckl, *Rev. Sci. Instrum.* **87**, 11D814 (2016).
- [33] L. Ballabio, J. Källne, and G. Gorini, *Nucl. Fusion* **38**, 1723 (1998).
- [34] B. Appelbe and J. Chittenden, *Plasma Phys. Control. Fusion* **53**, 045002 (2011).
- [35] B. Appelbe and J. Chittenden, *High Energy Density Phys.* **19**, 29 (2016).
- [36] C. J. Forrest, A. Deltuva, W. U. Schröder, A. V. Voinov, J. P. Knauer, E. M. Campbell, G. W. Collins, V. Y. Glebov, O. M. Mannion, Z. L. Mohamed, *et al.*, *Phys. Rev. C* **100**, 034001 (2019).
- [37] O. M. Mannion, V. Y. Glebov, C. J. Forrest, J. P. Knauer, V. N. Goncharov, S. P. Regan, T. C. Sangster, C. Stoeckl, and M. G. Johnson, *Rev. Sci. Instrum.* **89**, 10I131 (2018).
- [38] Z. L. Mohamed, O. M. Mannion, E. P. Hartouni, J. P. Knauer, and C. J. Forrest, *J. Appl. Phys.* **128**, 214501 (2020).
- [39] Z. L. Mohamed, O. M. Mannion, J. P. Knauer, C. J. Forrest, V. Y. Glebov, C. Stoeckl, and M. H. Romanofsky, *Rev. Sci. Instrum.* **92**, 043546 (2021).
- [40] T. Goorley, M. James, T. Booth, F. Brown, J. Bull, L. J. Cox, J. Durkee, J. Elson, M. Fensin, R. A. Forster, *et al.*, *Nucl. Technol.* **180**, 298 (2012).
- [41] C. Stoeckl, M. Cruz, V. Yu. Glebov, J. P. Knauer, R. Lauck, K. Marshall, C. Mileham, T. C. Sangster, and W. Theobald, *Rev. Sci. Instrum.* **81**, 10D302 (2010).
- [42] M. Gatun Johnson, A. B. Zylstra, A. Bacher, C. R. Brune, D. T. Casey, C. Forrest, H. W. Herrmann, M. Hohenberger, D. B. Sayre, R. M. Bionta, *et al.*, *Phys. Plasmas* **24**, 041407 (2017).
- [43] J. Delettretz, R. Epstein, M. C. Richardson, P. A. Jaanimagi, and B. L. Henke, *Phys. Rev. A* **36**, 3926 (1987).
- [44] D. T. Michel, S. X. Hu, A. K. Davis, V. Y. Glebov, V. N. Goncharov, I. V. Igumenshchev, P. B. Radha, C. Stoeckl, and D. H. Froula, *Phys. Rev. E* **95**, 051202 (2017).
- [45] R. Betti, K. Anderson, V. N. Goncharov, R. L. McCrory, D. D. Meyerhofer, S. Skupsky, and R. P. J. Town, *Phys. Plasmas* **9**, 2277 (2002).
- [46] A. Bose, R. Betti, D. Shvarts, and K. M. Woo, *Phys. Plasmas* **24**, 102704 (2017).
- [47] R. Nora, R. Betti, K. S. Anderson, A. Shvydky, A. Bose, K. M. Woo, A. R. Christopherson, J. A. Marozas, T. J. B. Collins, P. B. Radha, *et al.*, *Phys. Plasmas* **21**, 056316 (2014).
- [48] L. Spitzer, *Physics of fully ionized gases.*, 2nd ed. (Wiley Interscience, New York, 1962).
- [49] C. D. Zhou and R. Betti, *Phys. Plasmas* **14** (2007).
- [50] R. Betti, M. Umansky, V. Lobatchev, V. N. Goncharov, and R. L. McCrory, *Phys. Plasmas* **8**, 5257 (2001).
- [51] S. P. Regan, V. N. Goncharov, I. V. Igumenshchev, T. C. Sangster, R. Betti, A. Bose, T. R. Boehly, M. J. Bonino,

- E. M. Campbell, D. Cao, *et al.*, [Phys. Rev. Lett. **117**, 025001 \(2016\)](#).
- [52] V. N. Goncharov, S. P. Regan, T. C. Sangster, R. Betti, T. R. Boehly, E. M. Campbell, J. A. Delettrez, D. H. Edgell, R. Epstein, C. J. Forrest, *et al.*, [J. Phys. Conf. Ser. **717**, 012008 \(2016\)](#).
- [53] D. T. Casey, J. A. Frenje, M. Gatu Johnson, F. H. Séguin, C. K. Li, R. D. Petrasso, V. Y. Glebov, J. Katz, J. Magoon, D. D. Meyerhofer, *et al.*, [Rev. Sci. Instrum. **84**, 043506 \(2013\)](#).
- [54] “See Supplemental Material at URL for description of background model and error analysis on inferred values.”.
- [55] P. B. Radha, V. N. Goncharov, T. J. B. Collins, J. A. Delettrez, Y. Elbaz, V. Y. Glebov, R. L. Keck, D. E. Keller, J. P. Knauer, J. A. Marozas, *et al.*, [Phys. Plasmas **12**, 032702 \(2005\)](#).
- [56] I. V. Igumenshchev, V. N. Goncharov, W. T. Shmayda, D. R. Harding, T. C. Sangster, and D. D. Meyerhofer, [Phys. Plasmas **20**, 082703 \(2013\)](#).
- [57] I. V. Igumenshchev, A. L. Velikovich, V. N. Goncharov, R. Betti, E. M. Campbell, J. P. Knauer, S. P. Regan, A. J. Schmitt, R. C. Shah, and A. Shvydky, [Phys. Rev. Lett. **123**, 065001 \(2019\)](#).
- [58] R. C. Shah, S. X. Hu, I. V. Igumenshchev, J. Baltazar, D. Cao, C. J. Forrest, V. N. Goncharov, V. Gopalaswamy, D. Patel, F. Philippe, *et al.*, [Phys. Rev. E **103**, 023201 \(2021\)](#).
- [59] H. Zhang, R. Betti, R. Yan, and H. Aluie, [Phys. Plasmas **27**, 122701 \(2020\)](#).
- [60] S. X. Hu, D. T. Michel, A. K. Davis, R. Betti, P. B. Radha, E. M. Campbell, D. H. Froula, and C. Stoeckl, [Phys. Plasmas **23**, 102701 \(2016\)](#).
- [61] R. Betti, P. Y. Chang, B. K. Spears, K. S. Anderson, J. Edwards, M. Fatenejad, J. D. Lindl, R. L. McCrory, R. Nora, and D. Shvarts, [Phys. Plasmas **17**, 058102 \(2010\)](#).